Supporting Information Appendix for:

Effects of an HIV-1 Maturation Inhibitor on the Structure and Dynamics of CA-SP1 Junction Helices in Virus-Like Particles

Sebanti Gupta[†], John M. Louis, and Robert Tycko[*]
Laboratory of Chemical Physics
National Institute of Diabetes and Digestive and Kidney Diseases
National Institutes of Health
Bethesda, MD 20892-0520

[†]current address: Yenepoya Research Centre, Yenepoya University, Deralakatte, Mangalore 575018, Karnataka, India

[*]corresponding author: Dr. Robert Tycko, National Institutes of Health, Building 5, Room 409, Bethesda, MD 20892-0520. e-mail robertty@mail.nih.gov, phone 301-402-8272

Contents:

SI Methods (pages 2-7)

Theoretical expressions for $R_{1\rho}$ and R_2 relaxation rates (pages 8-13)

SI References (pages 14-15)

Table S1 (page 16)

Supporting Figures S1-S12 (pages 17-27)

SI Methods

Production of segmentally labeled ΔMA-CA-SP1-NC

The full ΔMA-CA-SP1-NC sequence is shown in Fig. S4A. This sequence includes a T287C substitution, which has been shown to increase the yield of VLPs (1). Our strategy for producing segmentally labeled ΔMA-CA-SP1-NC is depicted in Fig. S4B. As in earlier work on segmental labeling of HIV-1 CA (2), we used the split intein DnaE from *Nostoc punctiforme*, which is compatible with a variety of amino acid sequences at the splicing site and remains active under a variety of buffer conditions, including high denaturant concentrations (3, 4). ΔMA-CA-SP1-NC was produced by the trans-splicing reaction between two fusion protein constructs. The N-terminal fusion construct included residues 1-265 of ΔMA-CA-SP1-NC followed by the N-terminal intein segment of N*pu* DnaE. The C-terminal fusion construct included the C-terminal intein segment of N*pu* DnaE follwed by residues 266-348 of ΔMA-CA-SP1-NC. Because residue 266 is a native cysteine, no mutations in ΔMA-CA-SP1-NC were required.

In the folded state of HIV-1 CA, residue 266 (which is residue 218 of the CA sequence) is at the C-terminal end of helix H11 and is followed by the disordered C-terminal tail of CA. We therefore reasoned that this splicing site would be accessible for the trans-splicing reaction and would produce good yields of ligated product. Also, this choice of splicing site allowed us to leave most of CA unlabeled, minimizing congestion in ssNMR spectra. The N-terminal construct was cloned into the expression vector pET21 using NdeI and XhoI restriction sites. The C-terminal construct was cloned into a pET11a vector using NdeI and BamHI sites. The N-terminal and C-terminal constructs contain His_6 tags at their C-terminal and the N-terminal ends, respectively. This allowed the ligated product to be separated from unreacted constructs and from the refolded intein in a single step by affinity chromatography, simplifying purification of ligated ΔMA-CA-SP1-NC.

Transformed *Escherichia coli* BL21 (DE3) competent cells were added to 2.0 ml of Luria-Bertani (LB) medium with 100 μg/ml ampicillin, grown at 37° C for 3 h, transferred into 100 ml of either LB (for the unlabeled N-terminal construct) or isotopically labeled minimal medium (for the labeled C-terminal construct) to prepare the subculture, then grown overnight at 37° C. One liter of the minimal medium contained 33.2 ml of 30X salt solution (1 M Na_2HPO_4-$7H_2O$, 1 M KH_2PO_4, and 100 mM Na_2SO_4), 3.2 g of $^{13}C_6$-glucose, 1.5 g of $^{15}NH_4Cl$, 1 ml of 2 M $MgCl_2$, 100

μl of 2 M $CaCl_2$, 50 mg of thiamine, 10 ml of minimum essential medium (MEM) vitamin solution (100X) and 100 μg/ml of ampicillin. One liter of LB or minimal medium was inoculated with 100 ml of the overnight culture. The cells were grown at 37° C with shaking at 220 rpm. Protein expression was initiated by the addition of 0.5 mM isopropyl β- D-1-thiogalactopyranoside (IPTG) at an optical density (OD at 600 nm) of 0.8-1.2 for both constructs. After induction, cells were grown at 37° C for 4 h. The cells were harvested by centrifugation at 9000 rpm (12100 X g) for 30 min. The OD of the culture before harvesting was 2-3.5. Cell pellets were stored at -80° C. Approximately 120 mg of the N-terminal fusion construct or 45 mg of the C-terminal fusion construct was obtained from a one-liter culture (with LB medium or minimal medium, respectively).

For purification, cell pellets from each one-liter culture were resuspended in roughly 50 ml of lysis buffer [50 mM Tris, 500 mM NaCl, 1 mM tris(2-carboxyethyl)phosphine (TCEP), 1 tablet of EDTA-free Complete protease inhibitor (Roche), 200 μl of lysozyme from a stock of 20 mg/ml, pH 8.0]. The solution was sonicated (Branson model 250 sonifier, tapered horn with 3 mm diameter tip) at a duty cycle of 40% and an amplitude of 4 for 15 min, then incubated for 15 min at room temperature with 6 μl of nuclease (Pierce Universal Nuclease for Cell Lysis, ThermoFisher Scientific). The cell debris was pelleted by centrifugation at 18000 rpm (26500 X g) for 40 min. The pellet was then dissolved in buffer containing 50 mM Tris, 500 mM NaCl, 1 mM TCEP, 1 tablet of protease inhibitor and 7 M urea at pH 8.0 and pelleted again at 18000 rpm (26500 X g) for 40 min. The supernatant was purified by affinity chromatography on a Ni-NTA column (Qiagen). His_6-tagged fusion protein constructs were eluted with elution buffer (50 mM Tris, 500 mM NaCl, 1 mM TCEP, 400 mM imidazole, and 7 M urea, pH 8.0)

To initiate the trans-splicing reaction, eluted N-terminal and C-terminal constructs were mixed in a 1:1 molar ratio and dialyzed at room temperature for 40 h, using 30 ml dialysis bags with 3.5 kDa cutoff. The dialysis buffer contained 50 mM Tris, 500 mM NaCl, 1.0 mM TCEP, and 2.5 M urea at pH 6.8. Protein concentrations, estimated by UV absorption at 280 nm, were kept below 60 μM during dialysis. Samples for SDS-PAGE and reverse-phase high-performance liquid chromatography (HPLC) were taken at several time points to follow the ligation reaction. The protein mixture was then incubated with Ni-NTA beads, which had been equilibrated with dialysis buffer, and subsequently passed through a gravity column to remove intein proteins and unreacted fusion proteins. The purified ligated product, collected in the flow-through, was

refolded by overnight dialysis at 4° C against a buffer containing 50 mM Tris, 500 mM NaCl, and 1 mM TCEP at pH 6.8. The protein was chromatographed on a Hi-Trap SP-FF Sepharose column (GE Healthcare) and flow-through fractions were pooled and concentrated. The protein was further purified on a Superdex 75 10/300 GL size-exclusion column (GE Healthcare). Production of ligated ΔMA-CA-SP1-NC was confirmed by SDS-PAGE and mass spectrometry (Fig. S5). The final yield of ligated ΔMA-CA-SP1-NC was approximately 54% (*i.e.*, 22 mg of ligated product from a total of 60 mg of N-terminal and C-terminal fusion constructs in a 1:1 molar ratio).

Formation of VLPs with and without BVM

As previously described (1), VLPs were prepared at a final concentration of 10 mg/ml (260 μM) by mixing 600 μl of segmentally-labeled ΔMA-CA-SP1-NC in 30 mM MES at pH 6, 500 mM NaCl and 1 mM TCEP with 231 μl of 1.5 M tartrate and 92 μl of 1 M Tris, pH 7.5. This buffer composition is termed VLP-formation (VF) buffer. The resulting solution was incubated at 37° C for 2 h, followed by overnight incubation at room temperature. Formation of spherical ΔMA-CA-SP1-NC assemblies was verified by transmission electron microscopy (TEM).

To incorporate BVM (Millipore Sigma catalog number SML2057) into VLPs, a BVM stock solution at a concentration of 30 mg/ml was prepared in dimethyl sulfoxide (DMSO). This stock was gradually diluted over 2 h in VF buffer containing β-cyclodextrin to attain a clear solution with a final concentration of 500 μg/ml BVM (855 μM), 3% w/v β-cyclodextrin and 0.8% v/v DMSO. In this solution, the hydrophobic BVM molecules are solubilized by their containment within β-cyclodextrin cages. The BVM/β-cyclodextrin solution was then mixed with a suspension of preformed VLPs (10 mg/ml) in equal volumes to reach a final concentration of 130 μM ΔMA-CA-SP1-NC (as monomer) and 428 μM BVM. The mixture was incubated at room temperature for four days with occasional stirring to allow transfer of BVM from β-cyclodextrin cages to VLPs. Incorporation of BVM into VLPs was then verified by assays described below.

Preparation of mature HIV-1 protease

Cloning, expression and isolation of the active mature HIV-1 protease (PR) optimized for structural studies and enzyme kinetics via mutations (Q7K, L33I, L63I, C67A, C95A) to restrict self-degradation and prevent cysteine-thiol oxidation has been described previously (5). Induction for protein expression, isolation of inclusion bodies and protein purification followed previously

described protocols (6, 7). A stock solution of the folded PR in 25 mM sodium acetate at pH 5 (8) was diluted to the desired concentration in assay buffer.

Effect of BVM on PR-catalyzed cleavage of ΔMA-CA-SP1-NC in VLPs

PR was added to a suspension of VLPs in VF buffer, with a 1:10 molar ratio of PR to ΔMA-CA-SP1-NC. The solution was incubated at 24° C, and aliquots were taken for TEM analysis at various time points. TEM images (Figs. 1 and S1) were obtained with an FEI Morgagni microscope, operating at 80 keV. Negatively-stained samples were prepared on glow-discharged carbon films (Quantifoil grids, 2 nm film thickness). After diluting the VLP/PR aliquot by a factor of ten in VF buffer, a 10 µl volume was adsorbed to the carbon film for 30 s, then blotted with filter paper, rinsed with VF buffer, blotted, rinsed with deionized water, blotted, stained with 2% w/v uranyl acetate for 20-30 s, blotted, and dried in air.

To confirm directly that the effects on protein assembly morphologies seen in TEM images were due to effects on PR-catalyzed cleavage of ΔMA-CA-SP1-NC, processing of VLPs by PR was monitored by SDS-PAGE on 10-20% gradient Tris-Glycine gels (Fig S2). Reaction mixtures in VF buffer contained 36 µM ΔMA-CA-SP1-NC (in VLPs with or without BVM) and 1.38 µM PR. Aliquots (8 µl) were drawn at the indicated times and mixed with 4 µl of SDS-PAGE sample loading buffer, heated to 85° C for 2 min prior to electrophoresis. ΔMA-CA-SP1-NC and its cleavage products were visualized by staining the gel with Coomassie brilliant blue G-250 (Bio-Rad) and imaged.

Effect of BVM on PR activity and PR-catalyzed cleavage of unassembled Gag

Stock solutions (100 mM in DMSO) of BVM and the PR inhibitor darunavir (DRV) were diluted to 300 µM in 5 mM sodium acetate, pH 6, from which they were added to the assay mixture. Assays to test for inhibition of PR by BVM (Fig. S3A) were carried out in 50 mM sodium acetate buffer (pH 5) at a final concentration of 200 nM PR either in the absence or presence of BVM at 2.5 and 10 µM and 380 µM of the chromogenic substrate (9) Lys-Ala-Arg-Val-Nle-[4-nitrophenylalanine]-Glu-Ala-Nle-NH_2 (California Peptide Research) in a total volume of 120 µl at 28 ºC. A positive control for the inhibition of catalytic activity of PR was carried out using 1 µM of DRV.

Fig. S3A shows that BVM does not inhibit the catalytic activity of mature PR at 2.5 µM concentration in 50 mM acetate buffer at pH 5, or even up to 50-fold molar excess over PR significantly. The initial rate of cleavage of the chromogenic substrate is nearly identical either with or without BVM.

Assays (20 µl) to monitor cleavage of ΔGag, a truncated Gag construct that includes full-length MA, CA, SP1 and NC subunits, shown in Figs. S3B and S3C, were carried out at room temperature as described previously (10, 11). ΔGag (50 µM) in 20 mM sodium phosphate, pH 6.5, 300 mM NaCl, 0.1 mM $ZnCl_2$ and 1 mM TCEP was mixed with the PR to give a final concentration of 0.92 µM. Aliquots (2 µl) were drawn at the indicated times and mixed with 3 µl of the above assay buffer and 2 µl of SDS-PAGE sample loading buffer, heated to 85 °C for 2 min and subjected to electrophoresis on 4-20% gradient mini-protean TGX precast gel (Bio-Rad). ΔGag and its cleavage products were visualized either by exposing the gel to UV light (TGX gel) or by staining with Coomassie brilliant blue G-250 (Bio-Rad), and imaged. Reactions were also carried out in a final concentration of 10 µM BVM or 5 µM of DRV for the indicated times, followed by SDS-PAGE.

In Fig. S3C, BVM has no detectable effect on ΔGag processing by PR, and particularly on the cleavage between CA and SP1. Band intensities which signify the appearance and the disappearance of the CA-SP1 intermediate are similar in their time course (compare zoomed in view of blue and red boxes in Fig. S3C). A control digest in the presence of DRV at 5 µM shows complete inhibition as expected.

Solid state NMR

For ssNMR measurements, thin-wall 3.2 mm magic-angle spinning (MAS) rotors (Revolution NMR) were packed by ultracentrifugation with approximately 30 mg of sample, containing approximately 15 mg of VLPs without BVM or 10 mg of VLPs with BVM. Except for dipolar-shift correlation (DIPSHIFT) measurements, all ssNMR measurements were performed at 17.5 T (745.5 MHz ^{1}H NMR frequency) using a Varian InfinityPlus spectrometer console and a three-channel low-electric-field MAS NMR probe (Black Fox, LLC). An MAS frequency of 12.00 kHz was used. Sample temperatures were maintained at 10-12° C with cooled nitrogen gas in all measurements.

Two-dimensional (2D) and three-dimensional (3D) NCACX and NCOCX ssNMR spectra, as well as 2D ^{13}C-^{13}C ssNMR spectra, were obtained with standard methods, using cross-polarization for ^{1}H-^{15}N and ^{1}H-^{13}C polarization transfers (12), frequency-selective cross-polarization for ^{15}N-$^{13}C_{\alpha}$ and ^{15}N-^{13}CO polarization transfers (13), and dipolar-assisted rotational resonance (DARR) for ^{13}C-^{13}C polarization transfers (14). Two-pulse phase-modulated ^{1}H (TPPM) decoupling (15) with an 80 kHz ^{1}H radio-frequency (RF) field was applied during evolution and detection periods of 2D and 3D measurements. Other experimental parameters are given in Table S1. 2D and 3D spectra were analyzed and plotted with nmrPipe (16) and Sparky (https://www.cgl.ucsf.edu/home/sparky/) software. ^{13}C chemical shifts are relative to 2,2-dimethyl-2-silapentane-5-sulfonate (DSS), based on an external reference of 1-^{13}C-L-alanine powder at 179.65 ppm. ^{15}N chemical shifts are relative to liquid ammonia, based on the reported NMR frequency ratios for DSS and liquid ammonia (17).

^{15}N $T_{1\rho}$ and T_2 relaxation measurements were performed with RF pulse sequences in Figs. S9A and S9B, using 92 kHz continuous-wave ^{1}H decoupling during incremented ^{15}N spin-lock and spin-echo periods (τ_{SL} and τ_{echo}, respectively). A 40 kHz ^{15}N spin-locking field was used. These field strengths were found to give $T_{1\rho}$ data that are not affected by undesired ^{1}H-^{15}N cross-polarization or other extraneous effects. DARR mixing periods (τ_{mix}) were 50 ms in NCACX-detected measurements and 100 ms in NCOCX-detected measurements. Values of $T_{1\rho}$ and T_2 were derived from the experimental data by fitting with single-exponential decay functions in Origin software (OriginLab Corp.). Plots of $T_{1\rho}$ and T_2 for the diffusion-in-a-cone model in Figs. 4C and 4D are based on the theoretical expressions derived below.

^{15}N-^{1}H DIPSHIFT measurements (18-20) were performed at 14.1 T (599.2 MHz ^{1}H NMR frequency) with an MAS frequency of 7.00 kHz, using a Varian InfinityPlus spectrometer console and a three-channel BioMAS probe (Varian). These measurements were performed with the RF pulse sequence in Fig. S9C. ^{1}H homonuclear decoupling with the Lee-Goldburg (LG) technique (21) was applied during incremented dipolar evolution periods τ_{LG}, with an ^{1}H carrier frequency offset of 51.2 kHz and a ^{1}H RF field of 72.4 kHz. A DARR mixing period of 0.1 ms was used for data plotted in Fig. 5, and 30 ms for data plotted in Fig. S12. Simulations of DIPSHIFT data for Fig. 5 were performed with a custom-written program that calculates the evolution of isolated ^{1}H-^{15}N spin pairs under MAS, with ^{1}H-^{15}N dipole-dipole couplings acting only during τ_{LG} periods.

Theoretical expressions for $R_{1\rho}$ and R_2 relaxation rates

Although ^{15}N spin relaxation in ssNMR of proteins under MAS has been treated previously (22-25), we are not aware of explicit expressions for the dependence of orientationally-averaged ^{15}N $R_{1\rho}$ and R_2 relaxation rates on motional amplitude and diffusion constant in previous work. Therefore, expressions for orientationally-averaged ^{15}N $R_{1\rho}$ and R_2 relaxation rates under MAS are derived below with the assumption that these rates are determined only by fluctuations in one-bond ^{15}N-^{1}H magnetic dipole-dipole couplings due to molecular motions. Only fluctuations in the secular (*i.e.*, truncated) part of the dipole-dipole coupling are considered, as these are expected to dominate $R_{1\rho}$ and R_2 when motions occur on timescales greater than 100 ns.

We begin with a rotating-frame nuclear spin Hamiltonian (in units of rad/s) that includes the dipole-dipole coupling, which is time-dependent both due to MAS at frequency ω_R and due to molecular motions, and rf fields applied on-resonance with the ^{1}H spin (I, with gyromagnetic ratio γ_I) and the ^{15}N spin (S, with gyromagnetic ratio γ_S), with amplitudes ω_I and ω_S, respectively:

$$H(t) = d(t)I_zS_z + \omega_I I_x + \omega_S S_x \tag{1}$$

The dipole-dipole coupling strength is

$$d(t) = \sum_{m=-2}^{2} A_m(\alpha,\beta,\gamma;t)\exp(im\omega_R t) \tag{2}$$

with

$$\begin{aligned} A_{\pm 2} = \frac{\gamma_I\gamma_S\hbar}{8R^3}\{&\sin^2\theta[e^{2i\phi}(1\mp\cos\beta)^2e^{-2i\alpha} + e^{-2i\phi}(1\pm\cos\beta)^2e^{2i\alpha}] \\ &\pm 2\sin 2\theta[e^{i\phi}\sin\beta(1\mp\cos\beta)e^{-i\alpha} - e^{-i\phi}\sin\beta(1\pm\cos\beta)e^{i\alpha}] \\ &+2(3\cos^2\theta-1)\sin^2\beta\}e^{\pm 2i\gamma} \end{aligned} \tag{3a}$$

$$A_{\pm 1} = \mp \frac{\gamma_I \gamma_S \hbar}{2\sqrt{2} R^3} \{ \sin^2\theta [e^{2i\phi} \sin\beta (1 \mp \cos\beta) e^{-2i\alpha} - e^{-2i\phi} \sin\beta (1 \pm \cos\beta) e^{2i\alpha}]$$
$$+ \sin 2\theta [e^{i\phi} (1 \mp \cos\beta)(2\cos\beta \pm 1) e^{-i\alpha} - e^{-i\phi} (1 \pm \cos\beta)(2\cos\beta \mp 1) e^{i\alpha}] \qquad (3b)$$
$$\pm (3\cos^2\theta - 1) \sin 2\beta \} e^{\pm i\gamma}$$

and $A_0 = 0$. Euler angles α, β, and γ specify the orientation of a molecule-fixed axis system in the MAS rotor. Polar and azimuthal angles $\theta(t)$ and $\phi(t)$ specify the direction of the ^{15}N-^{1}H bond vector in the molecule-fixed axis system and are stochastically time-dependent due to molecular motion. R is the ^{15}N-^{1}H bond distance. In terms of second-rank spherical harmonics $Y_{2,m}(\theta,\phi)$ and reduced Wigner rotation matrix elements $d_{m,m'}^{(2)}(\beta)$,

$$A_m = \frac{\sqrt{6}\gamma_I \gamma_S \hbar}{R^3} \sum_{m'=-2}^{2} (-1)^{m'} Y_{2,m'}(\theta,\phi) d_{m,-m'}^{(2)}(-\beta) e^{-im'\alpha} d_{0,m}^{(2)}(-\theta_M) e^{im\gamma}, \quad \text{with} \quad \theta_M = \cos^{-1}(1/\sqrt{3}).$$

Note that $A_m^* = A_{-m}$.

In an interaction representation with respect to $\omega_I I_x + \omega_S S_x$, the Hamiltonian becomes

$$\tilde{H}(t) = d(t)[I_z S_z \cos\omega_I t \cos\omega_S t + I_y S_z \sin\omega_I t \cos\omega_S t$$
$$+ I_z S_y \cos\omega_I t \sin\omega_S t + I_y S_y \sin\omega_I t \sin\omega_S t] \qquad (4)$$

Following standard treatments of spin relaxation (26-28), $R_{1\rho}$ and R_2 are derived from a second-order approximate solution to the Liouville equation for the spin density operator $\rho(t)$ in this interaction representation, namely

$$\rho(t) \approx \rho(0) - i\int_0^t dt' [\tilde{H}(t'), \rho(0)] - \int_0^t dt' \int_0^{t'} dt'' [H(t'), [H(t''), \rho(0)]] \qquad (5)$$

Taking $\rho(0) = S_x$, which corresponds to an initial state of transverse S-spin magnetization along the x-axis of the rotating frame, the subsequent time-dependent amplitude of transverse magnetization becomes

$$\overline{\langle S_x(t)\rangle} = \mathrm{Tr}\{S_x\,\overline{\rho(t)}\}\big/\mathrm{Tr}\{S_x{}^2\} = 1 - \int_0^t dt' \int_0^{t'} dt''\,\overline{F(t',t'')} \tag{6}$$

Overlines in Eq. (6) denote ensemble averages over the trajectories of molecular motions, and

$$F(t',t'') = \frac{1}{4}[f_{zz}(t')f_{zz}(t'') + f_{yz}(t')f_{yz}(t'') + f_{zy}(t')f_{zy}(t'') + f_{yy}(t')f_{yy}(t'')] \tag{7}$$

with $f_{uv}(t)$ being the coefficient of $I_u S_v$ in $\tilde{H}(t)$.

In the general case, the right-hand side of Eq. (6) contains products of all pairs of terms in Eqs. (3a) and (3b), evaluated at t' and t''. However, if we consider molecular motion that is axially symmetric about an average N-H bond direction (for which $\theta = 0$), so that all values of $\phi(t)$ are equally probable at all times, then only terms proportional to $\sin^2\theta(t')\sin^2\theta(t'')\exp(\pm 2i[\phi(t') - \phi(t'')])$, $\sin 2\theta(t')\sin 2\theta(t'')\exp(\pm i[\phi(t') - \phi(t'')])$, and $[3\cos^2\theta(t') - 1][3\cos^2\theta(t'') - 1]$ survive in the ensemble average. The dependence on α also disappears. If in addition we average over γ, only terms proportional to $A_m(t')A_{-m}(t'')$ survive, and the dependence on the MAS frequency ω_R disappears.

$\overline{F(t',t'')}$ can be expressed as a sum of terms that depend on $\tau \equiv t' - t''$ and/or $\eta = t' + t''$. This is true because, with the assumption that the motion is a stationary random process, the following correlation functions depend only on τ:

$$C_0(\tau) \equiv \frac{1}{4}\overline{[3\cos^2\theta(t') - 1][3\cos^2\theta(t'') - 1]} \tag{8a}$$

$$\begin{aligned} C_1(\tau) &\equiv \frac{3}{8}\overline{\sin 2\theta(t')\sin 2\theta(t'')\exp(\pm i[\phi(t') - \phi(t'')])} \\ &= \frac{3}{8}\overline{\sin 2\theta(t')\sin 2\theta(t'')\cos([\phi(t') - \phi(t'')])} \end{aligned} \tag{8b}$$

$$\begin{aligned} C_2(\tau) &\equiv \frac{3}{8}\overline{\sin^2\theta(t')\sin^2\theta(t'')\exp(\pm 2i[\phi(t') - \phi(t'')])} \\ &= \frac{3}{8}\overline{\sin^2\theta(t')\sin^2\theta(t'')\cos(2[\phi(t') - \phi(t'')])} \end{aligned} \tag{8c}$$

Moreover, $\cos\omega_I t' = \cos\frac{\omega_I\tau}{2}\cos\frac{\omega_I\eta}{2} - \sin\frac{\omega_I\tau}{2}\sin\frac{\omega_I\eta}{2}$, etc. Importantly, only a subset of the terms in $\overline{F(t',t'')}$ makes contributions to the right-hand side of Eq. (6) that grow linearly with t at large values of t. This subset consists of the terms that depend only on τ (and do not depend on η) and decay to zero with increasing τ. Other terms make oscillatory contributions that do not grow with t at large values of t. Defining $G(\tau)$ to be the sum of terms in $\overline{F(t',t'')}$ that depend only on τ and decay to zero with increasing τ, it is readily shown that

$$\begin{aligned}\int_0^t dt' \int_0^{t'} dt'' G(\tau) &= \int_0^t d\tau (t-\tau) G(\tau) \\ &\approx t\int_0^\infty d\tau G(\tau)\end{aligned} \tag{9}$$

The approximation in the second line is valid when t is large compared to the decay time of $G(\tau)$. The transverse spin relaxation rate is then $\int_0^\infty d\tau G(\tau)$.

Using Eqs. (3), (4), (7), and (8), it can then be shown that

$$\begin{aligned}G(\tau) = &\left(\frac{\gamma_I\gamma_S\hbar}{R^3}\right)^2 \{[C_2(\tau)-C_2(\infty)][\frac{(1-\cos\beta)^4+(1+\cos\beta)^4}{96} + \frac{\sin^2\beta[(1-\cos\beta)^2+(1+\cos\beta)^2]}{12}] \\ &+[C_1(\tau)-C_1(\infty)][\frac{\sin^2\beta[(1-\cos\beta)^2+(1+\cos\beta)^2]}{24} + \frac{(1-\cos\beta)^2(2\cos\beta+1)^2+(1+\cos\beta)^2(2\cos\beta-1)^2}{12}] \\ &+[C_0(\tau)-C_0(\infty)][\frac{\sin^4\beta}{16}+\frac{\sin^2 2\beta}{8}]\}[\cos(\omega_I+\omega_S)\tau+\cos(\omega_I-\omega_S)\tau] \\ = &\left(\frac{\gamma_I\gamma_S\hbar}{R^3}\right)^2 \{[C_2(\tau)-C_2(\infty)][\frac{9+6\cos^2\beta-7\cos^4\beta}{48}] + [C_1(\tau)-C_1(\infty)][\frac{3-6\cos^2\beta+7\cos^4\beta}{12}] \\ &+[C_0(\tau)-C_0(\infty)][\frac{1+6\cos^2\beta-7\cos^4\beta}{16}]\}[\cos(\omega_I+\omega_S)\tau+\cos(\omega_I-\omega_S)\tau]\end{aligned} \tag{10}$$

The orientationally-averaged transverse spin relaxation rate is then

$$\int_0^\infty d\tau \int_0^\pi d\beta \sin\beta G(\tau) = \left(\frac{\gamma_I \gamma_S \hbar}{R^3}\right)^2 \int_0^\infty d\tau \{\frac{1}{5}[C_2(\tau) - C_2(\infty)] + \frac{1}{5}[C_1(\tau) - C_1(\infty)] + \frac{1}{10}[C_0(\tau) - C_0(\infty)]\}[\cos(\omega_I + \omega_S)\tau + \cos(\omega_I - \omega_S)\tau] \quad (11)$$

To proceed further, we use the approximate expressions for $C_m(\tau)$ derived by Lipari and Szabo (29) for orientational diffusion of a vector within a cone of half-angle θ_0, according to which $C_m(\tau) - C_m(\infty) \approx X_m \exp(-\tau / \tau_m)$ with

$$X_0 = \frac{1}{20}[x_0(1+x_0)(9x_0^2 - 1) + 4] - \frac{1}{4}x_0^2(1+x_0)^2 \quad (12a)$$

$$X_1 = \frac{1}{10}(1-x_0)[(2+x_0)(1+3x_0^2) + 3x_0] \quad (12b)$$

$$X_2 = \frac{1}{40}(1-x_0)^2(3x_0^2 + 9x_0 + 8) \quad (12c)$$

$$\tau_0 = \frac{1}{D_w X_0}\left\{\frac{x_0^2(1+x_0)^2}{2(x_0 - 1)}[\ln\frac{(1+x_0)}{2} - \frac{(1-x_0)}{2}] + \frac{(1-x_0)(2 - x_0 - 9x_0^2 - 7x_0^3)}{60}\right\} \quad (13a)$$

$$\tau_1 = \frac{(1-x_0)^2(9 + 32x_0 + 44x_0^2 + 20x_0^3)}{120 D_w X_1} \quad (13b)$$

$$\tau_2 = \frac{(1-x_0)^3(8 + 12x_0 + 5x_0^2)}{240 D_w X_2} \quad (13c)$$

where $x_0 \equiv \cos\theta_0$ and D_w is the orientational diffusion constant. As usual, D_w is defined such that an orientation distribution that is proportional to a second-rank spherical harmonic function decays exponentially with characteristic time $(6D_w)^{-1}$ when the diffusion is fully isotropic (*i.e.*, when $\theta_0 = \pi$). (Note that the expression in the original Lipari-Szabo paper (29) that corresponds to Eq. 13a contains a typographical error.) With these single-exponential approximations for the correlation functions, the orientationally averaged relaxation rates become

$$R_{1\rho} = \left(\frac{\gamma_I \gamma_S \hbar}{R^3}\right)^2 \left\{ \frac{X_2 \tau_2}{5} \left(\frac{1}{1+(\omega_I+\omega_S)^2 \tau_2^{\,2}} + \frac{1}{1+(\omega_I-\omega_S)^2 \tau_2^{\,2}} \right) \right.$$
$$\left. + \frac{X_1 \tau_1}{5} \left(\frac{1}{1+(\omega_I+\omega_S)^2 \tau_1^{\,2}} + \frac{1}{1+(\omega_I-\omega_S)^2 \tau_1^{\,2}} \right) + \frac{X_0 \tau_0}{10} \left(\frac{1}{1+(\omega_I+\omega_S)^2 \tau_0^{\,2}} + \frac{1}{1+(\omega_I-\omega_S)^2 \tau_0^{\,2}} \right) \right\}$$

(14)

$$R_2 = \left(\frac{\gamma_I \gamma_S \hbar}{R^3}\right)^2 \left(\frac{2X_2 \tau_2}{5(1+\omega_I^{\,2} \tau_2^{\,2})} + \frac{2X_1 \tau_1}{5(1+\omega_I^{\,2} \tau_1^{\,2})} + \frac{X_0 \tau_0}{5(1+\omega_I^{\,2} \tau_0^{\,2})} \right) \qquad (15)$$

With R in Å units, $\frac{\gamma_I \gamma_S \hbar}{R^3} = \frac{76504}{R^3}$ s^{-1} for a ^{15}N-^{1}H dipole-dipole coupling.

SI references

1. M. J. Bayro, B. K. Ganser-Pornillos, K. K. Zadrozny, M. Yeager, R. Tycko, Helical conformation in the CA-SP1 junction of the immature HIV-1 lattice determined from solid-state NMR of virus-like particles. *J. Am. Chem. Soc.* **138**, 12029-12032 (2016).
2. S. Gupta, R. Tycko, Segmental isotopic labeling of HIV-1 capsid protein assemblies for solid state NMR. *J. Biomol. NMR* **70**, 103-114 (2018).
3. J. Zettler, V. Schütz, H. D. Mootz, The naturally split Npu DnaE intein exhibits an extraordinarily high rate in the protein trans-splicing reaction. *FEBS Lett.* **583**, 909-914 (2009).
4. H. Iwai, S. Züger, J. Jin, P. H. Tam, Highly efficient protein trans-splicing by a naturally split DnaE intein from Nostoc punctiforme. *FEBS Lett.* **580**, 1853-1858 (2006).
5. J. M. Louis, G. M. Clore, A. M. Gronenborn, Autoprocessing of HIV-1 protease is tightly coupled to protein folding. *Nat. Struct. Biol.* **6**, 868-875 (1999).
6. J. M. Sayer, J. Agniswamy, I. T. Weber, J. M. Louis, Autocatalytic maturation, physical/chemical properties, and crystal structure of group N HIV-1 protease: Relevance to drug resistance. *Protein Sci.* **19**, 2055-2072 (2010).
7. J. M. Louis, R. Ishima, A. Aniana, J. M. Sayer, Revealing the dimer dissociation and existence of a folded monomer of the mature HIV-2 protease. *Protein Sci.* **18**, 2442-2453 (2009).
8. R. Ishima, D. A. Torchia, J. M. Louis, Mutational and structural studies aimed at characterizing the monomer of HIV-1 protease and its precursor. *J. Biol. Chem.* **282**, 17190-17199 (2007).
9. A. D. Richards, L. H. Phylip, W. G. Farmerie, P. E. Scarborough, A. Alvarez, B. M. Dunn, P. H. Hirel, J. Konvalinka, P. Strop, L. Pavlickova, V. Kostka, J. Kay, Sensitive, soluble chromogenic substrates for HIV-1 proteinase. *J. Biol. Chem.* **265**, 7733-7736 (1990).
10. L. Deshmukh, J. M. Louis, R. Ghirlando, G. M. Clore, Transient HIV-1 Gag-protease interactions revealed by paramagnetic NMR suggest origins of compensatory drug resistance mutations. *Proc. Natl. Acad. Sci. U.S.A.* **113**, 12456-12461 (2016).
11. J. M. Louis, L. Deshmukh, J. M. Sayer, A. Aniana, G. M. Clore, Mutations proximal to sites of autoproteolysis and the α-helix that co-evolve under drug pressure modulate the autoprocessing and vitality of HIV-1 protease. *Biochemistry* **54**, 5414-5424 (2015).
12. A. Pines, M. G. Gibby, J. S. Waugh, Proton-enhanced NMR of dilute spins in solids. *J. Chem. Phys.* **59**, 569-590 (1973).
13. M. Baldus, A. T. Petkova, J. Herzfeld, R. G. Griffin, Cross polarization in the tilted frame: Assignment and spectral simplification in heteronuclear spin systems. *Mol. Phys.* **95**, 1197-1207 (1998).
14. K. Takegoshi, S. Nakamura, T. Terao, ^{13}C-^{1}H dipolar-assisted rotational resonance in magic-angle spinning NMR. *Chem. Phys. Lett.* **344**, 631-637 (2001).
15. A. E. Bennett, C. M. Rienstra, M. Auger, K. V. Lakshmi, R. G. Griffin, Heteronuclear decoupling in rotating solids. *J. Chem. Phys.* **103**, 6951-6958 (1995).
16. F. Delaglio, S. Grzesiek, G. W. Vuister, G. Zhu, J. Pfeifer, A. Bax, Nmrpipe: A multidimensional spectral processing system based on Unix pipes. *J. Biomol. NMR* **6**, 277-293 (1995).

17. D. S. Wishart, C. G. Bigam, J. Yao, F. Abildgaard, H. J. Dyson, E. Oldfield, J. L. Markley, B. D. Sykes, ^{1}H, ^{13}C and ^{15}N chemical shift referencing in biomolecular NMR. *J. Biomol. NMR* **6**, 135-140 (1995).
18. S. D. Cady, M. Hong, Amantadine-induced conformational and dynamical changes of the influenza M2 transmembrane proton channel. *Proc. Natl. Acad. Sci. U.S.A.* **105**, 1483-1488 (2008).
19. J. X. Lu, W. M. Yau, R. Tycko, Evidence from solid-state NMR for nonhelical conformations in the transmembrane domain of the amyloid precursor protein. *Biophys. J.* **100**, 711-719 (2011).
20. M. G. Munowitz, R. G. Griffin, G. Bodenhausen, T. H. Huang, Two-dimensional rotational spin-echo nuclear magnetic-resonance in solids: Correlation of chemical shift and dipolar interactions. *J. Am. Chem. Soc.* **103**, 2529-2533 (1981).
21. M. Lee, W. I. Goldburg, Nuclear magnetic resonance line narrowing by a rotating rf field. *Physical Review* **140**, 1261-1271 (1965).
22. J. M. Lamley, M. J. Lougher, H. J. Sass, M. Rogowski, S. Grzesiek, J. R. Lewandowski, Unraveling the complexity of protein backbone dynamics with combined ^{13}C and ^{15}N solid-state NMR relaxation measurements. *PCCP* **17**, 21997-22008 (2015).
23. P. Schanda, B. H. Meier, M. Ernst, Quantitative analysis of protein backbone dynamics in microcrystalline ubiquitin by solid-state NMR spectroscopy. *J. Am. Chem. Soc.* **132**, 15957-15967 (2010).
24. N. Giraud, M. Blackledge, M. Goldman, A. Bockmann, A. Lesage, F. Penin, L. Emsley, Quantitative analysis of backbone dynamics in a crystalline protein from nitrogen-15 spin-lattice relaxation. *J. Am. Chem. Soc.* **127**, 18190-18201 (2005).
25. A. Krushelnitsky, T. Zinkevich, B. Reif, K. Saalwachter, Slow motions in microcrystalline proteins as observed by MAS-dependent ^{15}N rotating-frame NMR relaxation. *J. Magn. Reson.* **248**, 8-12 (2014).
26. R. K. Wangsness, F. Bloch, The dynamical theory of nuclear induction. *Physical Review* **89**, 728-739 (1953).
27. A. G. Redfield, On the theory of relaxation processes. *IBM Journal of Research and Development* **1**, 19-31 (1957).
28. A. Abragam, *The principles of nuclear magnetism* (Oxford University Press, Oxford, 1961).
29. G. Lipari, A. Szabo, Pade approximants to correlation functions for restricted rotational diffusion. *J. Chem. Phys.* **75**, 2971-2976 (1981).

Table S1: Conditions for 2D and 3D ssNMR measurements on ΔMA-CA-SP1-NC VLPs. Measurements were performed at 17.5 T (187.51 MHz ^{13}C NMR frequency, 75.56 MHz ^{15}N NMR frequency) with MAS at 12.00 kHz.

spectrum	measurement conditions
2D NCACX	100.8 μs t_1 increment, 80 complex t_1 points, 10.0 μs t_2 increment, 512 complex t_2 points, 25 ms ^{13}C-^{13}C DARR period, 1.5 s recycle delay, 768[a] or 1280[b] scans per FID
2D NCOCX	100.8 μs t_1 increment, 80 complex t_1 points, 10.0 μs t_2 increment, 512 complex t_2 points, 50 ms ^{13}C-^{13}C DARR period, 1.5 s recycle delay, 768[a] or 1280[b] scans per FID
2D ^{13}C-^{13}C	15.0 μs t_1 increment, 214 complex t_1 points, 10.0 μs t_2 increment, 512 complex t_2 points, 25 ms ^{13}C-^{13}C DARR period, 1.5 s recycle delay, 96 scans per FID
3D NCACX	100.8 μs t_1 increment, 50 complex t_1 points, 75.6 μs t_2 increment, 42 t_2 complex t_2 points, 10.0 μs t_3 increment, 512 complex t_2 points, 25 ms ^{13}C-^{13}C DARR period, 1.5 s recycle delay, 32 scans per FID
3D NCOCX	100.8 μs t_1 increment, 50 complex t_1 points, 75.6 μs t_2 increment, 42 t_2 complex t_2 points, 10.0 μs t_3 increment, 512 complex t_2 points, 25 ms ^{13}C-^{13}C DARR period, 1.5 s recycle delay, 32 scans per FID

[a]VLPs without BVM; [b]VLPs with BVM

Supporting Figures

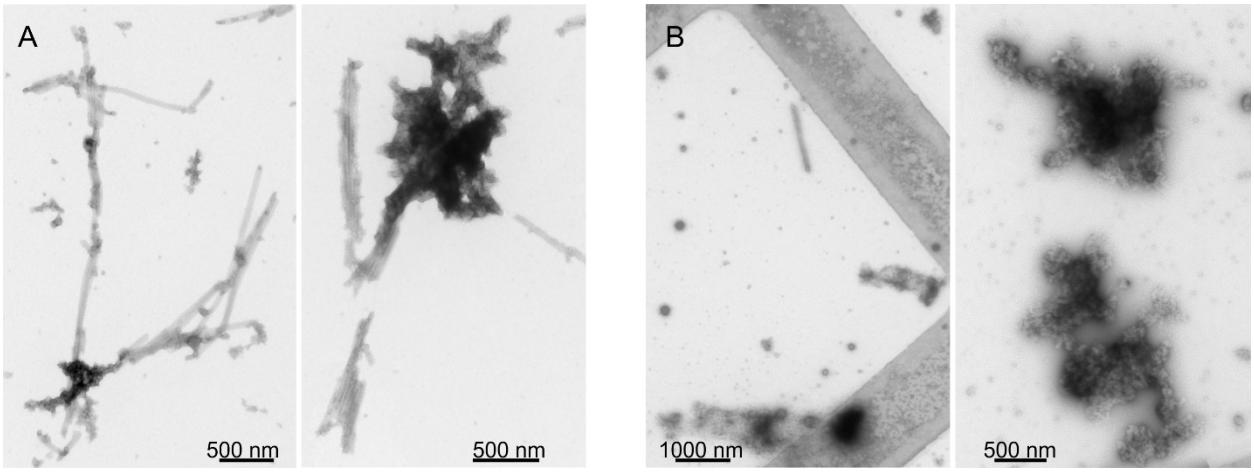

Figure S1: TEM images of VLPs with and without BVM after treatment with PR for 48 h.

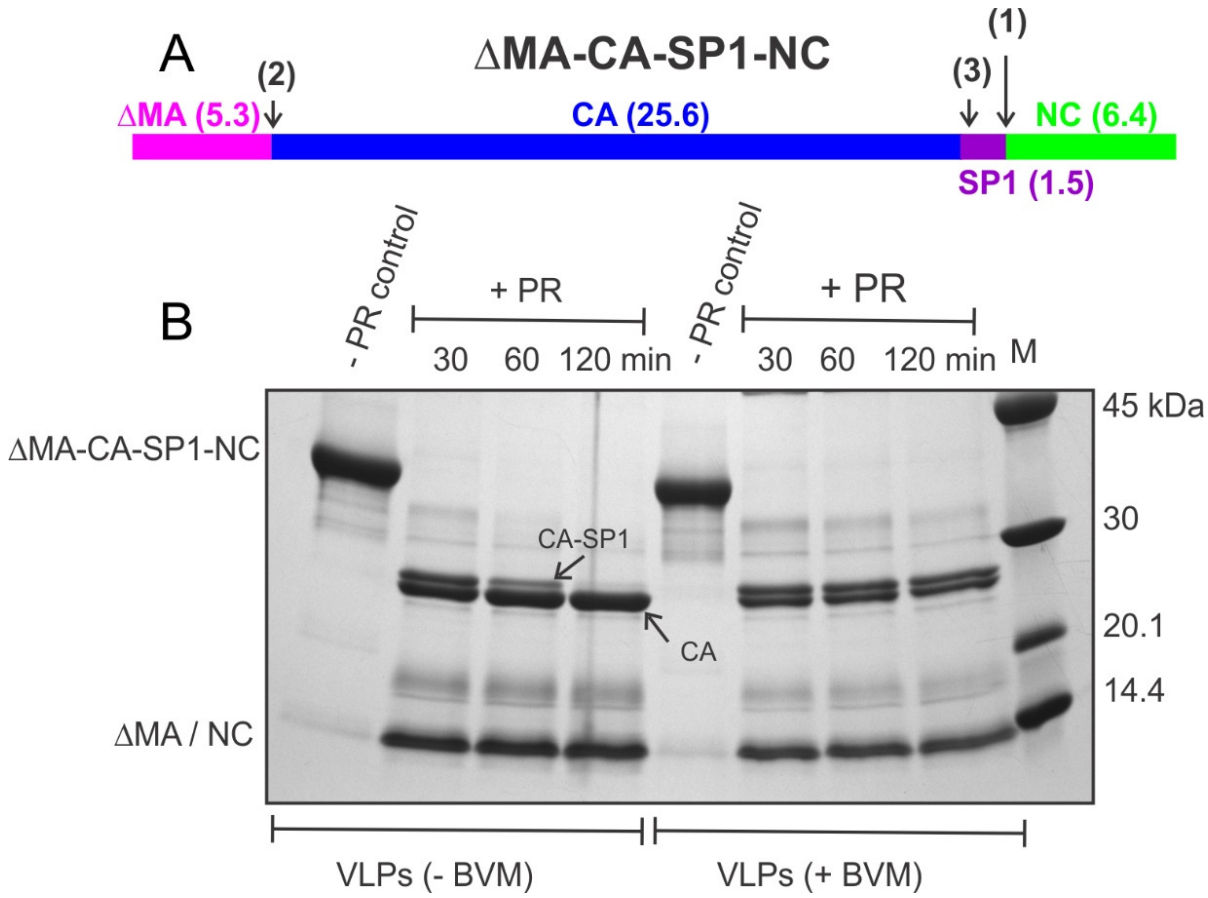

Figure S2: (A) Schematic representation of the sequential PR-catalyzed cleavages of ΔMA-CA-SP1-NC in VLPs, with the order of cleavage (numbers in parentheses), cleavage site positions (black arrows), and molecular weights of the products (kDa) indicated. (B) Time course of processing of VLPs by PR monitored by SDS-PAGE on a 10-20% gradient Tris-Glycine gel. Molecular weight markers are in the lane marked M. After 30 min, cleavage steps 1 and 2 are nearly complete, producing the intermediate product CA-SP1. From 30 to 120 min, in the absence of BVM, CA-SP1 is almost completely cleaved to produce CA. In the presence of BVM, CA-SP1 remains uncleaved at 120 min. (The constant CA band in the presence of BVM is attributable to unassembled ΔMA-CA-SP1-NC, which is fully cleaved before 30 min, and which constitutes approximately 30% of the ΔMA-CA-SP1-NC in the reaction mixtures under the conditions of these experiments.)

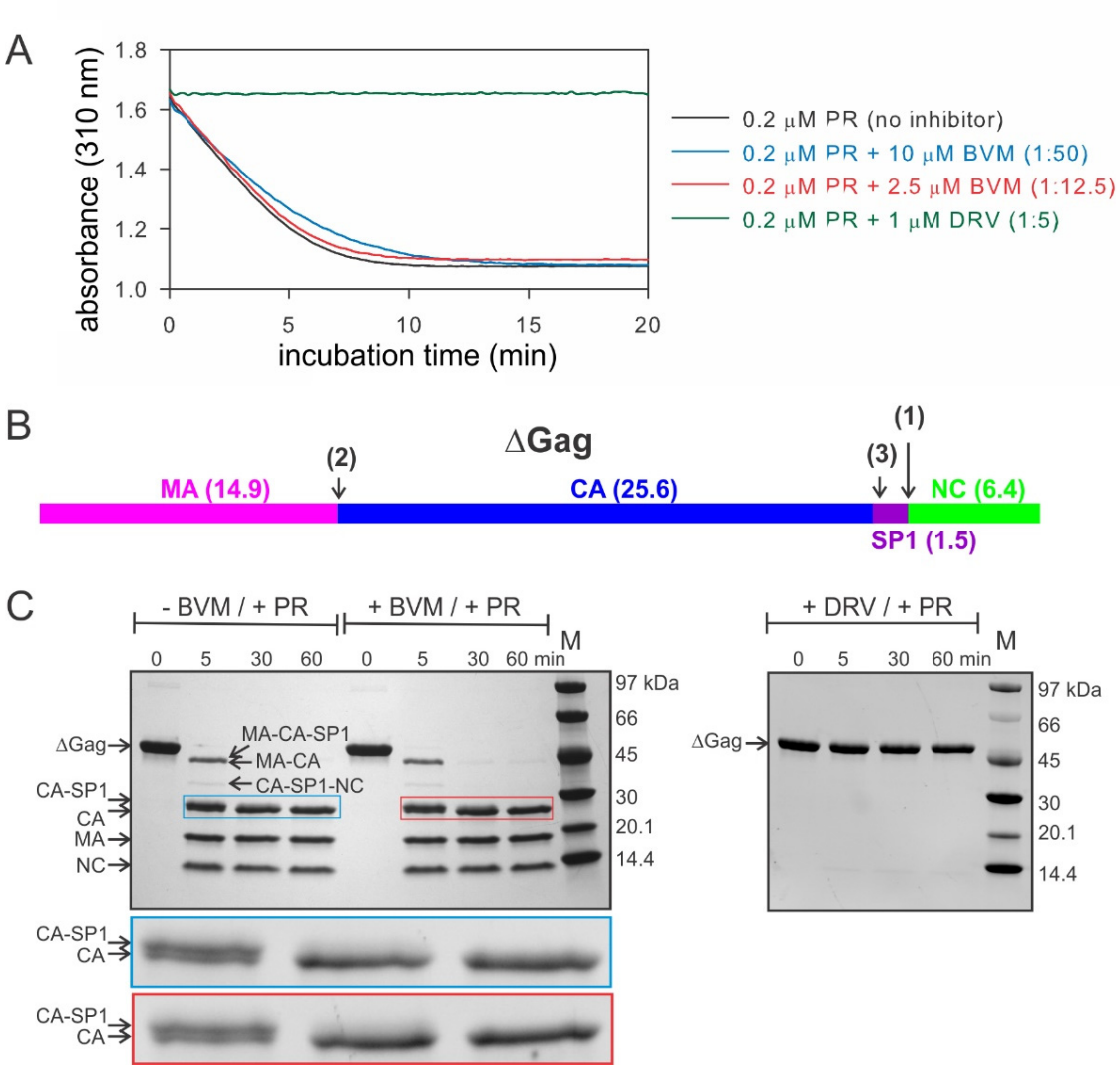

Figure S3: (A) Time-dependent absorbance due to PR-catalyzed cleavage of a chromogenic substrate at the indicated concentrations of PR and BVM. BVM has little direct effect on PR activity. Complete inhibition of activity by DRV (green trace) is shown as positive control. (B) Schematic representation of the sequential PR-catalyzed cleavages of ΔGag, with the order of cleavage (numbers in parentheses), cleavage site positions (black arrows), and molecular weights of the products (kDa) indicated. (C) Time course of processing of unassembled ΔGag by PR monitored by SDS-PAGE on 4-20% gradient mini-protean TGX gel. Molecular weight markers are in the lane marked M, Reaction mixtures contained 50 μM unassembled ΔGag (*i.e.*, no VLPs) and 0.92 μM PR in the absence or presence of BVM (10 μM). Cleavage of full length 48.4 kDa ΔGag (left panel) between SP1 and NC (step 1) yields MA-CA-SP1 + NC, followed by cleavage between MA and CA (step 2) to generate MA and the intermediate CA-SP1. SP1 is cleaved subsequently (slowest step 3) from the C-terminus of CA-SP1, roughly half of which is still detectable just above the CA band at 5 min. No full-length ΔGag or CA-SP1 remains at 5 and 30 min, respectively. The time course is nearly identical in the absence or presence of BVM, as seen in the expanded regions outlined in blue or red, respectively. As a positive control, 5 μM darunavir (DRV) completely blocks PR-catalyzed cleavage of ΔGag (right panel).

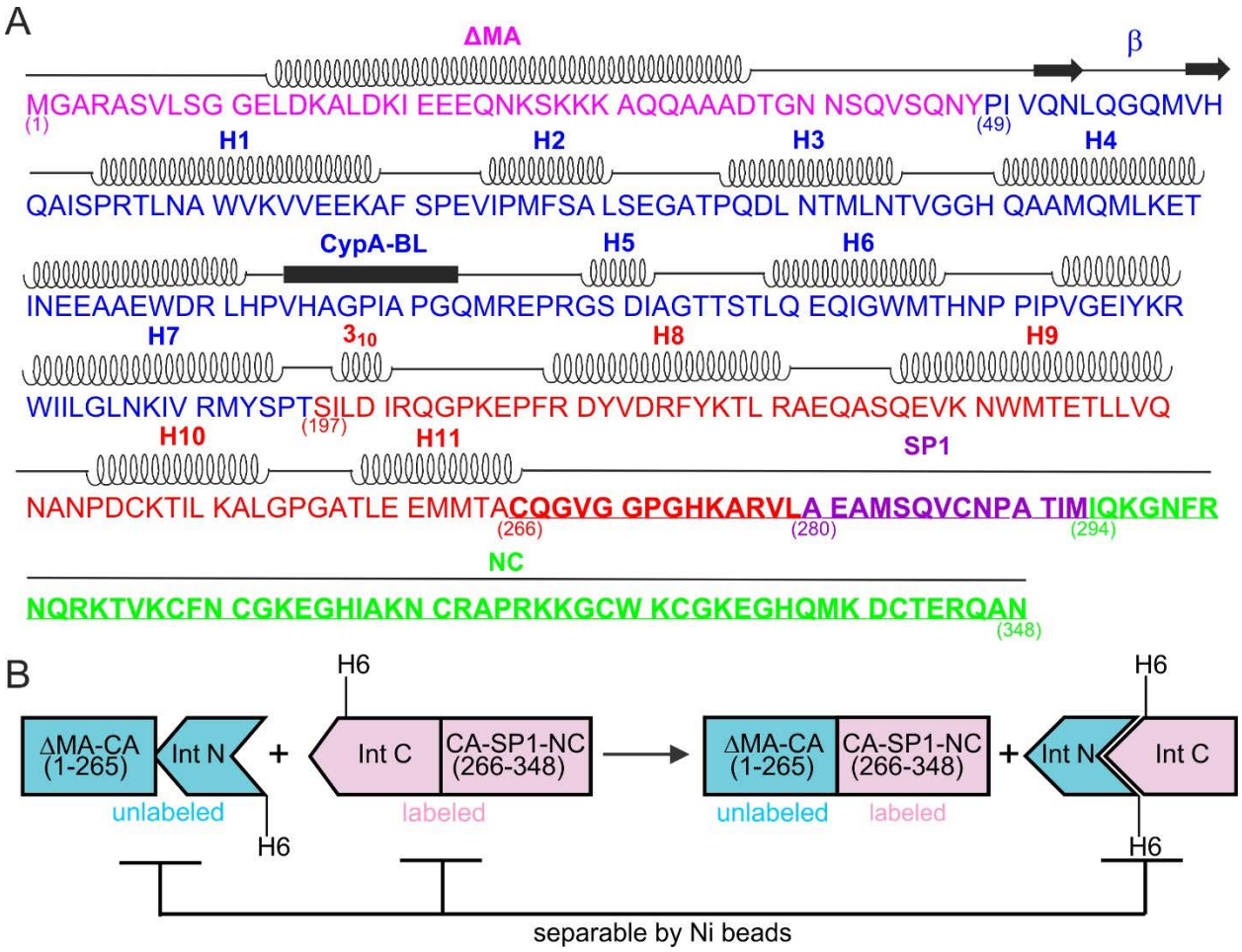

Figure S4: Strategy for production of segmentally labeled ΔMA-CA-SP1-NC. (A) Amino acid sequence, with ΔMA in magenta, N-terminal domain of CA in blue, C-terminal domain of CA in red, SP1 in purple, and NC in green. The β-hairpin segment, α-helical segments H1-H11, cyclophilin A binding loop, and 3_{10} helical segment of CA are indicated. (B) His_6-tagged fusion proteins, consisting of residues 1-265 of ΔMA-CA-SP1-NC fused to the N-terminal intein domain and residues 266-348 of ΔMA-CA-SP1-NC fused to the C-terminal intein domain, undergo trans-splicing to produce segmentally labeled, full-length ΔMA-CA-SP1-NC. The full-length intein and unreacted fusion proteins are removed by affinity chromatography.

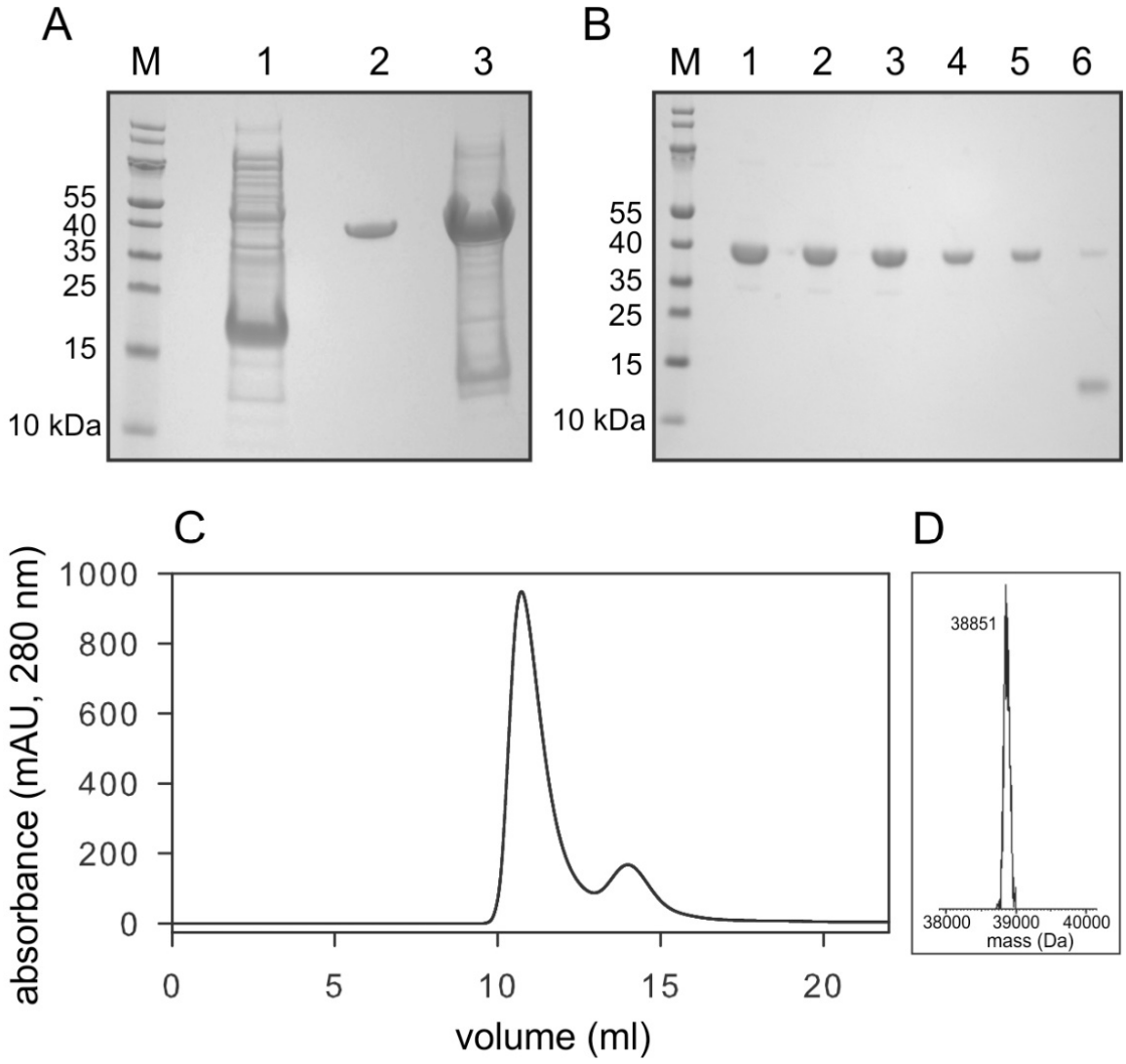

Figure S5: (A) SDS-PAGE analysis of the cell lysate from over-expression of the ΔMA-CA-IntN construct (lane 3, 42.2 kDa), the cell lysate from over-expression of the IntC-CA-SP1-NC construct (lane 1, 15.1 kDa), and purified, segmentally-labelled ΔMA-CA-SP1-NC (lane 2, 38.9 kDa). Molecular weight markers are in the lane marked M. (B) SDS-PAGE analysis of fractions from the first chromatographic purification step, using a Hi-Trap SP-FF Sepharose column. Fractions containing ΔMA-CA-SP1-NC are in lanes 2-6. The unbound fraction is in lane 6. Gels were stained using Imperial protein stain. (C) Chromatogram from the second purification step, using a Superdex 75 10/300 GL column. The main peak contains segmentally-labeled ΔMA-CA-SP1-NC. (D) Mass spectrum of the main peak after deconvolution of multi-charged m/z data from electrospray ionization.

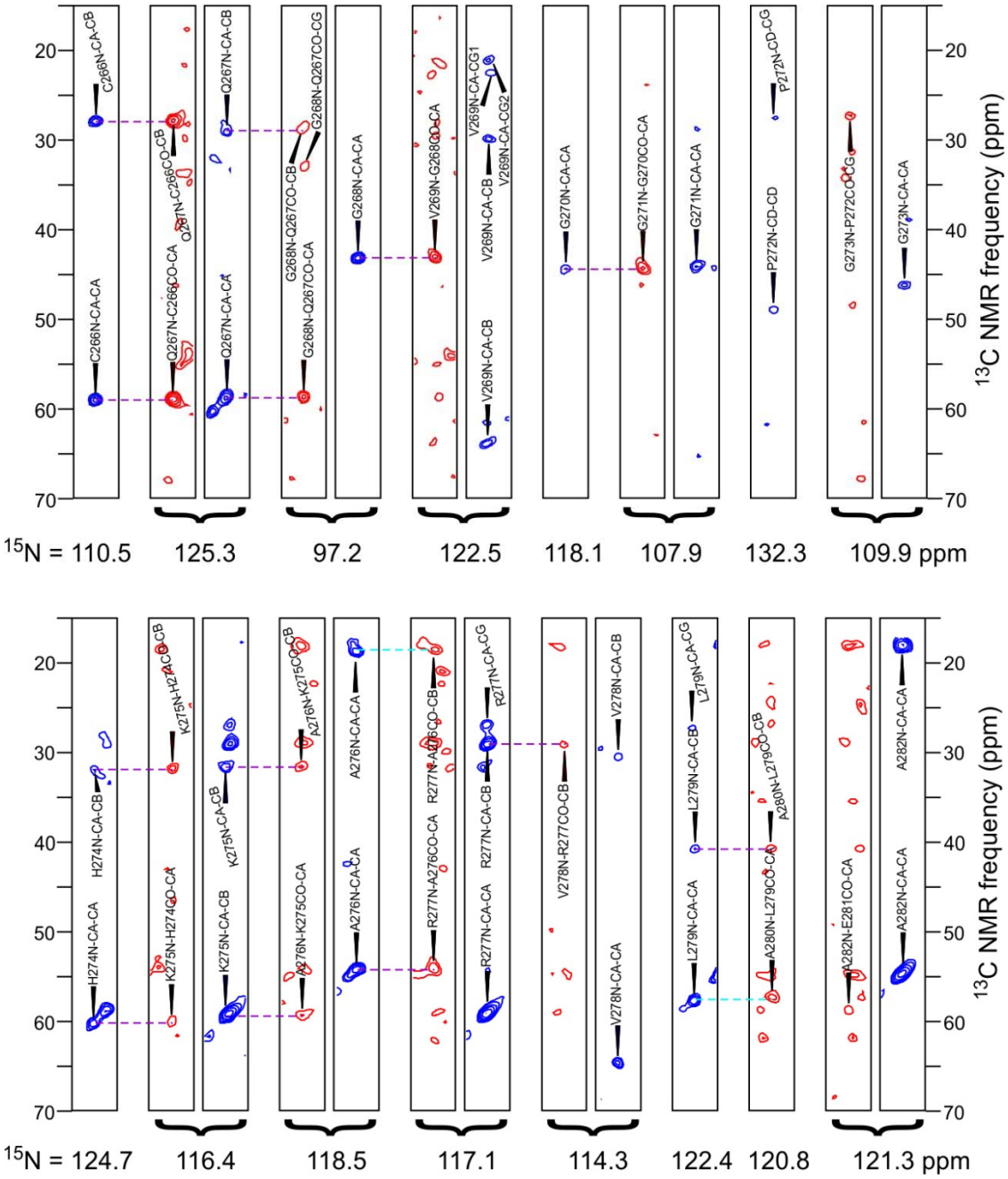

Figure S6: Portions of 2D planes (*i.e.*, "strip plots") from the 3D NCACX spectrum (blue contours) and the 3D NCOCX spectrum (red contours) of segmentally labeled VLPs without BVM. ^{13}C-^{13}C planes are taken at the indicated ^{15}N frequencies in the t_1 dimension, with the t_2 dimension on the horizontal axis and the t_3 dimension on the vertical axis. In the t_2 dimension, each strip is centered at the $^{13}C_\alpha$ frequency of the labeled crosspeaks and has a width of 5 ppm. Contour levels increase by successive factors of 1.3. Site-specific assignments are derived from a combination of these 3D spectra and the 2D spectra in Fig. 2. Dashed purple lines indicate connections that support these assignments.

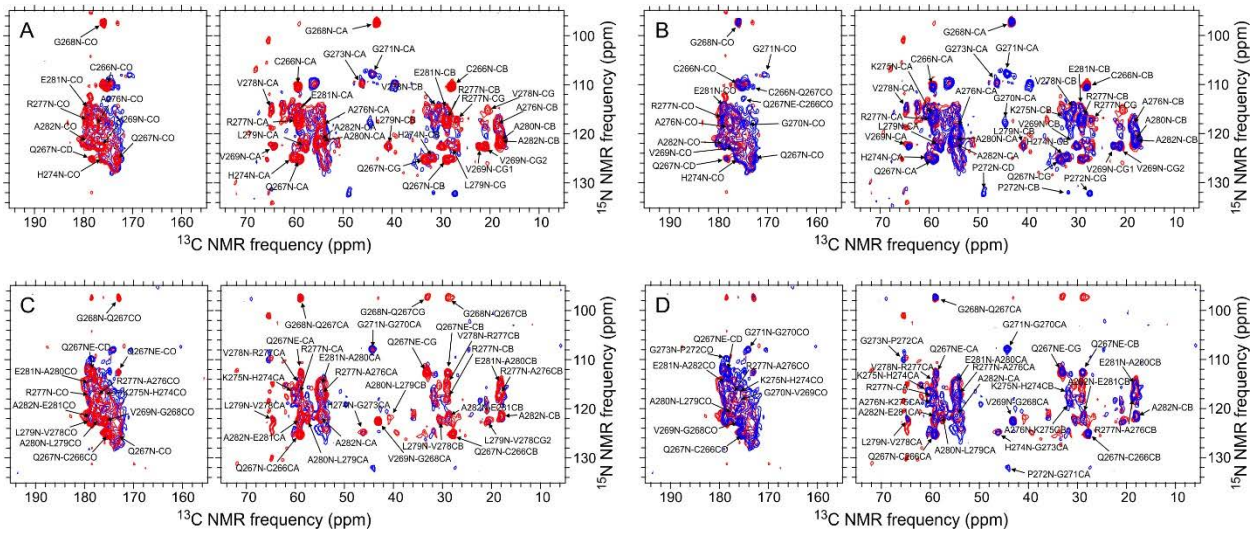

Figure S7: Superpositions of 2D NCACX (A,B) and NCOCX (C,D) spectra of segmentally-labeled VLPs with and without BVM. In panels A and C, contours for VLPs with BVM (red) are displayed over counters for VLPs without BVM (blue). Assignments refer to 2D spectra of VLPs with BVM. In panels B and D, contours for VLPs without BVM (blue) are displayed over counters for VLPs with BVM (red). Assignments refer to 2D spectra of VLPs without BVM. Contour levels increase by successive factors of 1.3.

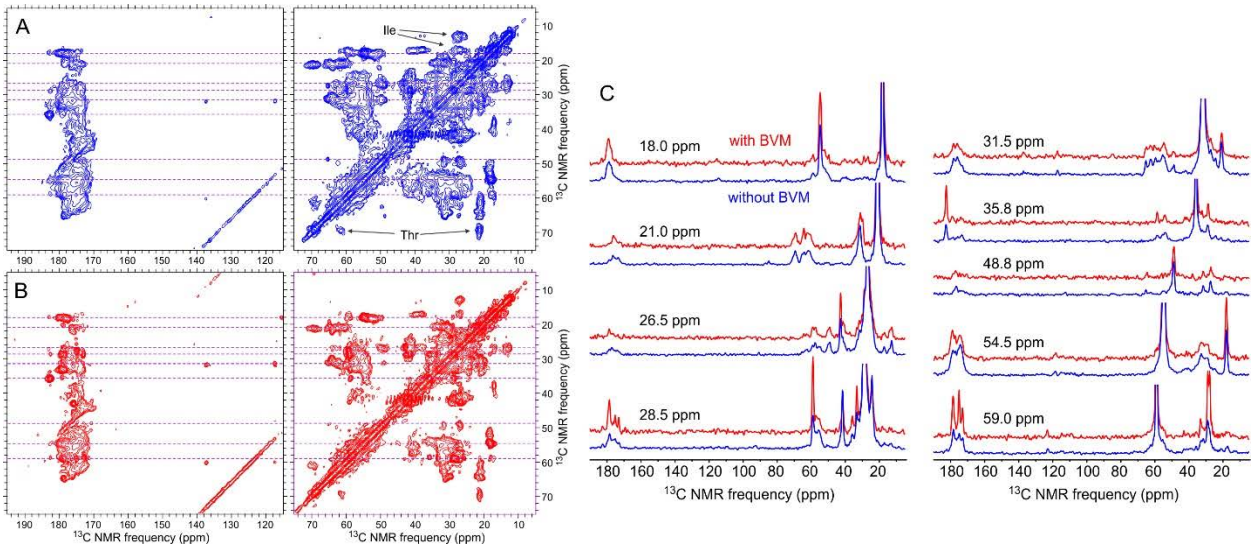

Figure S8: 2D ^{13}C-^{13}C spectra of segmentally-labeled VLPs without (A, blue contours) and with (B, red contours) BVM. Contour levels increase by successive factors of 1.4. (C) 1D slices from the 2D ^{13}C-^{13}C spectra, taken at the dashed purple lines in panels A and B.

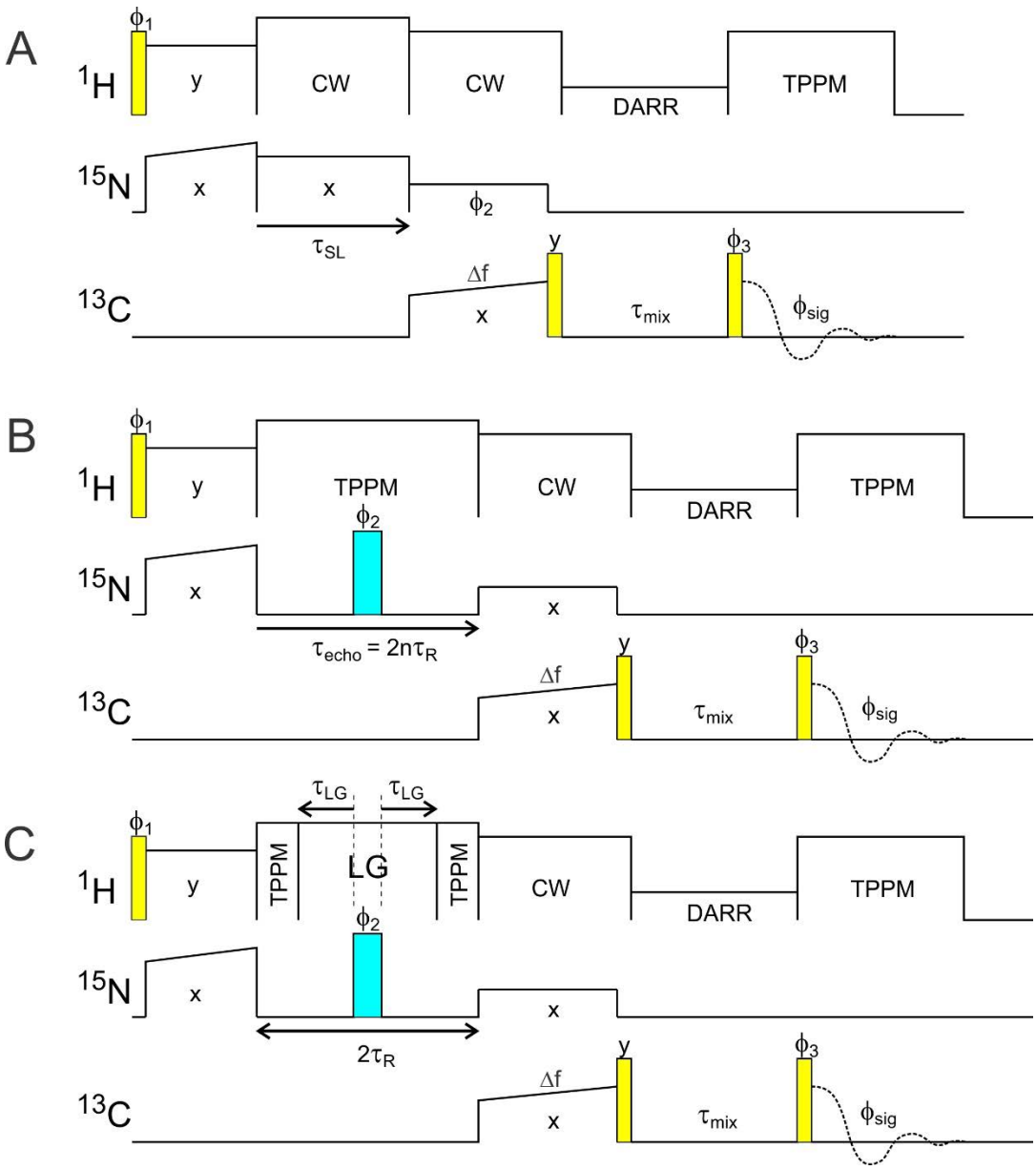

Figure S9: Radio-frequency pulse sequences for ^{13}C-detected ^{15}N $T_{1\rho}$ measurements (A), ^{15}N T_2 measurements (B), and DIPSHIFT measurements of ^{15}N-^{1}H dipole-dipole couplings (C). Yellow and cyan rectangles are $\pi/2$ and π pulses, respectively. ^{13}C carrier frequency offsets Δf are adjusted to select ^{15}N-^{13}CO or ^{15}N-$^{13}C_\alpha$ cross-polarization transfers, for NCOCX-detected or NCACX-detected measurements. MAS rotation, ^{13}C-^{13}C polarization transfer, ^{15}N spin-locking, ^{15}N spin-echo, and ^{1}H-^{1}H Lee-Goldburg decoupling periods are τ_R, τ_{mix}, τ_{SL}, τ_{echo}, and τ_{LG}, respectively. Other abbreviations are: CW = continuous wave decoupling; TPPM = two-pulse phase-modulated decoupling; DARR = dipolar-assisted rotational resonance. Phase cycling in panel A includes: ϕ_1 = x,-x; ϕ_2 = x,x,-x,-x; ϕ_3 = x,x,x,x,y,y,y,y; ϕ_{sig} = x,-x,-x,x,y,-y,-y,y. Phase cycling in panels B and C includes: ϕ_1 = x,-x; ϕ_2 = x,x,y,y,-x,-x,-y,-y; ϕ_3 = x,x,x,x,x,x,x,x,y,y,y,y,y,y,y,y; ϕ_{sig} = x,-x,-x,x,x,-x,-x,x,y,-y,-y,y, y,-y,-y,y.

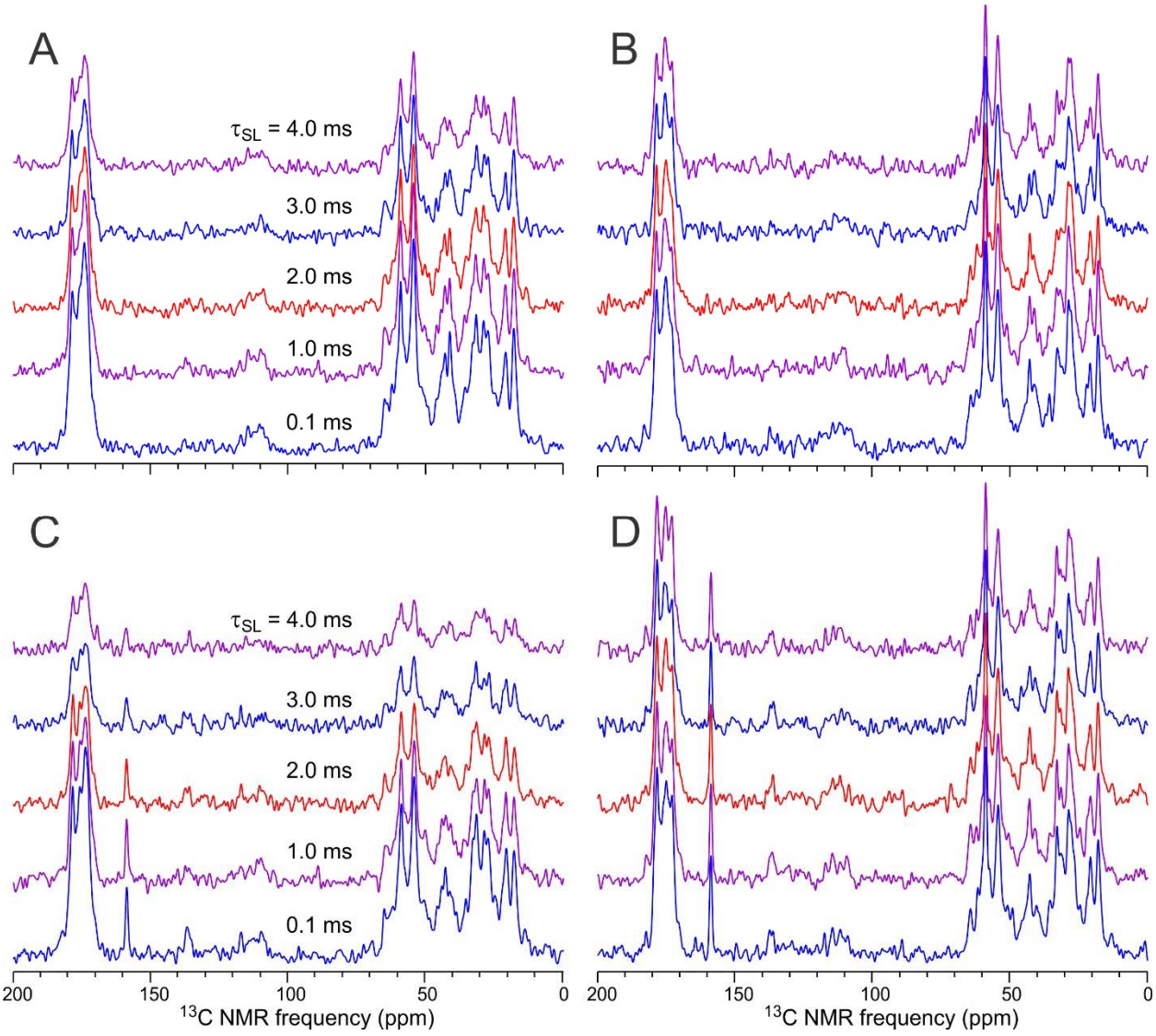

Figure S10: 1D ^{13}C spectra from ^{15}N $T_{1\rho}$ measurements. (A) VLPs without BVM, NCACX-detected. (B) VLPs with BVM, NCACX-detected. (C) VLPs without BVM, NCOCX-detected. (D) VLPs with BVM, NCOCX-detected.

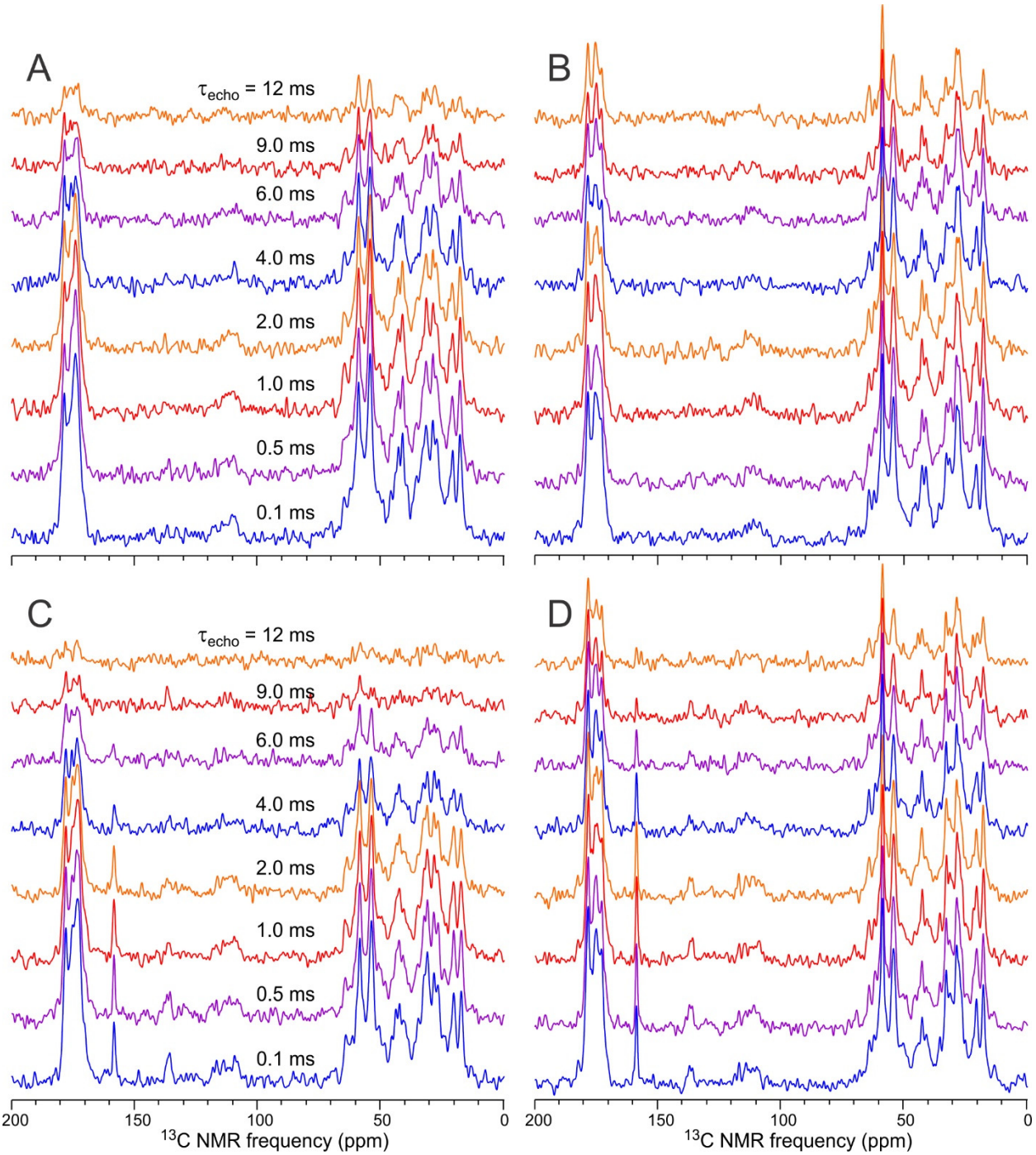

Figure S11: 1D ^{13}C spectra from ^{15}N T_2 measurements. (A) VLPs without BVM, NCACX-detected. (B) VLPs with BVM, NCACX-detected. (C) VLPs without BVM, NCOCX-detected. (D) VLPs with BVM, NCOCX-detected.

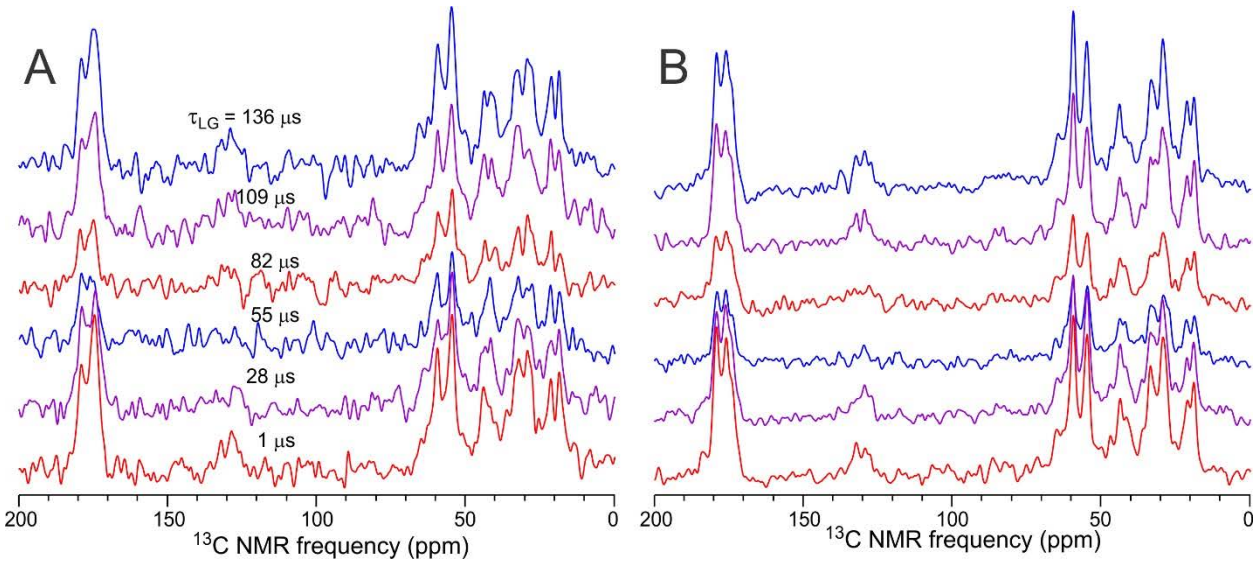

Figure S12: 1D ^{13}C spectra from NCACX-detected ^{15}N-^{1}H DIPSHIFT measurements on VLPs without BVM (A) and VLPs with BVM (B).

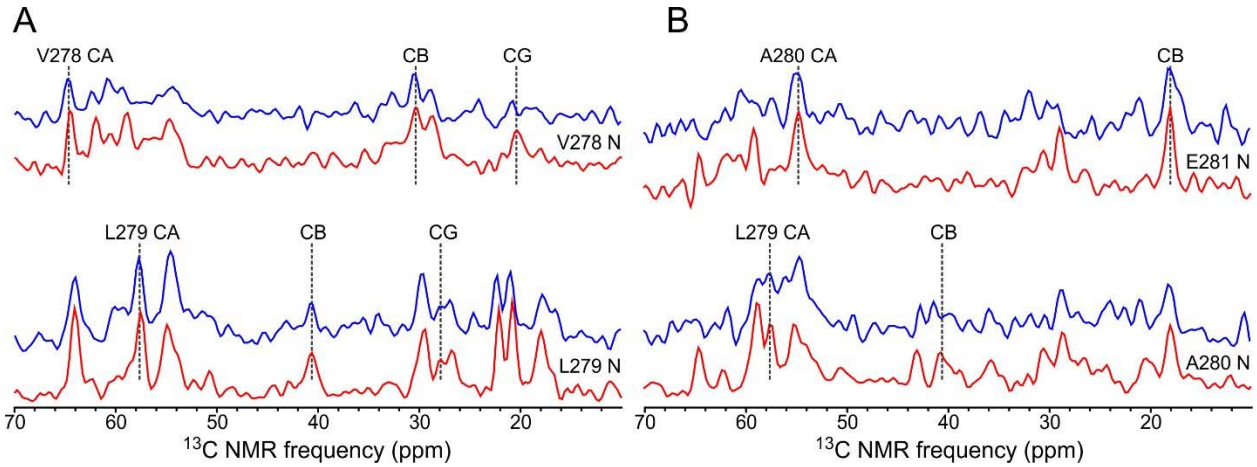

Figure S13: 1D slices from 2D NCACX (A) and NCOCX (B) spectra at ^{15}N NMR frequencies of V278, L279, A280, or E281. The full 2D spectra are shown in Fig. 2. Slices from spectra of VLPs with BVM (red) and without BVM (blue) are compared, and ^{13}C NMR frequencies of V278, L279, and A280 are indicated by vertical dashed lines.